Journal of Power Sources 248 (2014) 615–620

Contents lists available at ScienceDirect

Journal of Power Sources

journal homepage: www.elsevier.com/locate/jpowsour

Electrochemical properties of $LiMn_xFe_{1-x}PO_4$ ($x = 0$, 0.2, 0.4, 0.6, 0.8 and 1.0)/vapor grown carbon fiber core–sheath composite nanowire synthesized by electrospinning method

Koichi Kagesawa [a], Eiji Hosono [a,*], Masashi Okubo [a], Daisuke Nishio-Hamane [b], Tetsuichi Kudo [a], Haoshen Zhou [a]

[a] National Institute of Advanced Industrial Science and Technology (AIST), Umezono 1-1-1, Tsukuba, Ibaraki 305-8568, Japan
[b] Institute for Solid State Physics, The University of Tokyo, Kashiwanoha 5-1-5, Kashiwa, Chiba 277-8581, Japan

HIGHLIGHTS

- Nonwoven structured $LiMn_xFe_{1-x}PO_4$/VGCF nanowires are prepared.
- $LiMn_xFe_{1-x}PO_4$ nanowires consist of a single crystal.
- $LiMn_xFe_{1-x}PO_4$ nanowires are covered by amorphous carbon.
- Fe ratio in $LiMn_xFe_{1-x}PO_4$ is important for good performance.

ARTICLE INFO

Article history:
Received 12 July 2013
Received in revised form
25 September 2013
Accepted 30 September 2013
Available online 7 October 2013

Keywords:
Core–sheath nanowire
$LiMn_xFe_{1-x}PO_4$4/VGCF
Electrospinning
High-power Li-ion battery

ABSTRACT

Core–sheath composite nanowires of $LiMn_xFe_{1-x}PO_4$ ($x = 0$, 0.2, 0.4, 0.6, 0.8 and 1.0) with vapor grown carbon fiber (VGCF) were synthesized by an electrospinning method. X-ray diffraction, SEM and TEM revealed that the electrospinning method could successfully fabricate a VGCF core at the nanowire-structured $LiMn_xFe_{1-x}PO_4$ sheath covered with an amorphous carbon layer. Furthermore, the spot patterns by selected area electron diffraction confirmed that $LiMn_xFe_{1-x}PO_4$ sheath consists of bundles of single-crystalline nanowire. The nanowire-structured electrode materials with uniformly dispersed carbon and highly crystalline active materials provided excellent rate capability.

1. Introduction

Recently, there have been numerous efforts devoted to realizing high-power Li-ion batteries for application to electric vehicles and plug-in hybrid vehicles [1,2]. Nanostructured cathode materials are one of the most effective ways to achieve high power because the short Li-ion diffusion length and the large solid/electrolyte interface area can improve the high charge/discharge rate capacity [3,4]. However, although the nanoparticulate materials can be synthesized easily, they frequently undergo aggregation, which reduces the surface area. Moreover, there is generally a severe trade-off between the nano-structure fabrication and high crystallinity; high-temperature heating for high crystallinity incurs undesirable grain growth.

A nonwoven cloth structure consisting of one-dimensional (1D) nanowire could suppress both aggregation and grain growth during high-temperature heating, and we have been focusing on an electrospinning method for the fabrication of 1D nanowire cathode materials. The electrospinning method can fabricate nanowires through easy and simple procedures [5–10]: A polymer solution is placed in a syringe with a needle. When the electric potential reaches a critical level, the electrostatic force causes the drawing out of a fine jet, which then whips toward the grounded target and creates dry nanowires through the drying of the solvent during the electrospinning process between the needle and the target. The nanowires are collected on the target.

In this work, we apply the electrospinning method to olivine type solid-solution $LiMn_xFe_{1-x}PO_4$. Olivine type $LiMPO_4$ (M = Mn,

* Corresponding author.
E-mail address: e-hosono@aist.go.jp (E. Hosono).

0378-7753/$ – see front matter © 2013 Elsevier B.V. All rights reserved.
http://dx.doi.org/10.1016/j.jpowsour.2013.09.133

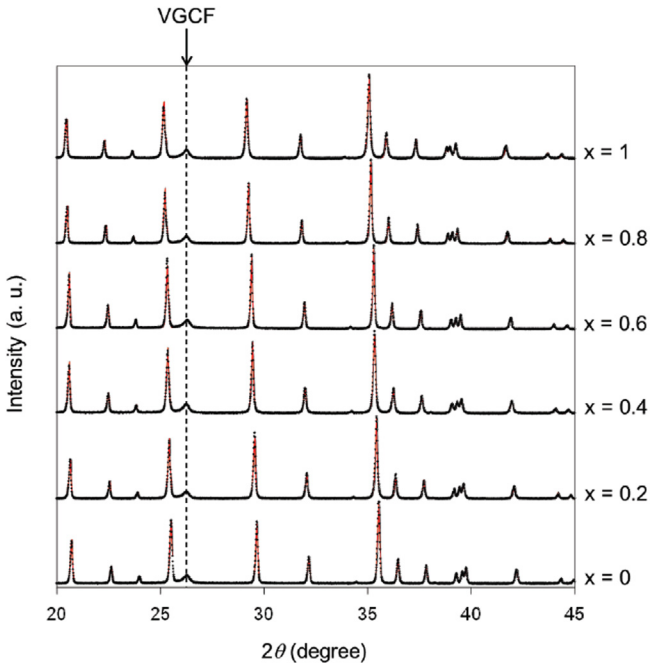

Fig. 1. Rietveld refinement pattern of the X-ray diffraction data for $LiMn_xFe_{1-x}PO_4$ (space group *Pnma*) with VGCF. The observed intensity data are shown by dots; the red solid lines overlying them are the calculated intensity. (For interpretation of the references to colour in this figure legend, the reader is referred to the web version of this article.)

Fe) is a promising cathode material [11,12] because of the relatively high energy density comparable to that of $LiCoO_2$ and low cost by the use of abundant Fe and Mn. In addition, polyanion materials generally have higher thermal stability than transition-metal oxide cathode materials [13–15]. However, $LiMPO_4$ has low ionic and electronic conductivities, which strongly limits the electrode performance [16–18]. Therefore, nanostructuring of $LiMn_xFe_{1-x}PO_4$ is mandatory to optimize both energy and power densities [17,19].

In this study, we report the synthesis and electrochemical properties of the 1D nanowire $LiMn_xFe_{1-x}PO_4$ (x = 0, 0.2, 0.4, 0.6, 0.8 and 1). The resultant $LiMn_xFe_{1-x}PO_4$ was used as the active material of a lithium ion battery and the influences of the nanostructuring and composition were evaluated in detail.

2. Experiment

2.1. Materials

A series of $LiMn_xFe_{1-x}PO_4$/VGCF was prepared as described in a previous paper [20]. Stoichiometric $LiNO_3$, $Mn(NO_3)_2 \cdot 6H_2O$, $Fe(NO_3)_3 \cdot 9H_2O$, $NH_4H_2PO_4$ and polyacrylic acid were dissolved in a mixed solution of water, methanol and nitric acid. After stirring for 1 h, the VGCF was ultrasonically dispersed in the solution using a sonohorn. The resultant precursor solution was poured into a syringe connected to a metal needle. A direct current electric field of 25 kV was applied between the needle and the Al foil target used as a collector. The as-spun materials were dried in a vacuum for 1 h at 100 °C, after which the dried materials separated from the Al foil were heated at 800 °C for 10 h under Ar flow.

2.2. Characterization

Crystallographic structural characterization was performed by X-ray powder diffraction (XRD) and Rietveld refinement. The XRD analysis was carried out on a Rigaku SmartLab X-ray diffractometer using Cu $K\alpha$ radiation. The morphology was observed by means of field-emission scanning electron microscopy (FE-SEM) and bright-field transmission electron microscopy (bright-field TEM) using a Carl Zeiss Gemini and a JEOL JEM-2010F (200 kV accelerating voltage), respectively.

Electrochemical measurements were performed using a three-electrode cell. The active materials were mixed and

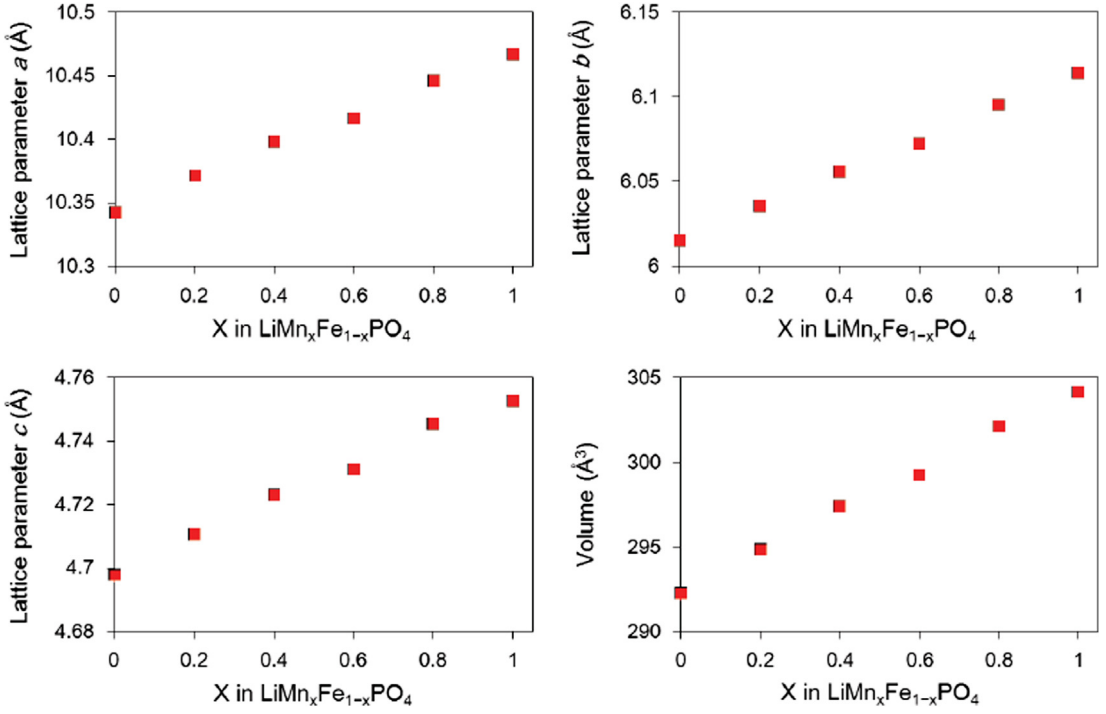

Fig. 2. Variation of lattice constants and unit cell volume as a function of LiMn content x in $Mn_xFe_{1-x}PO_4$.

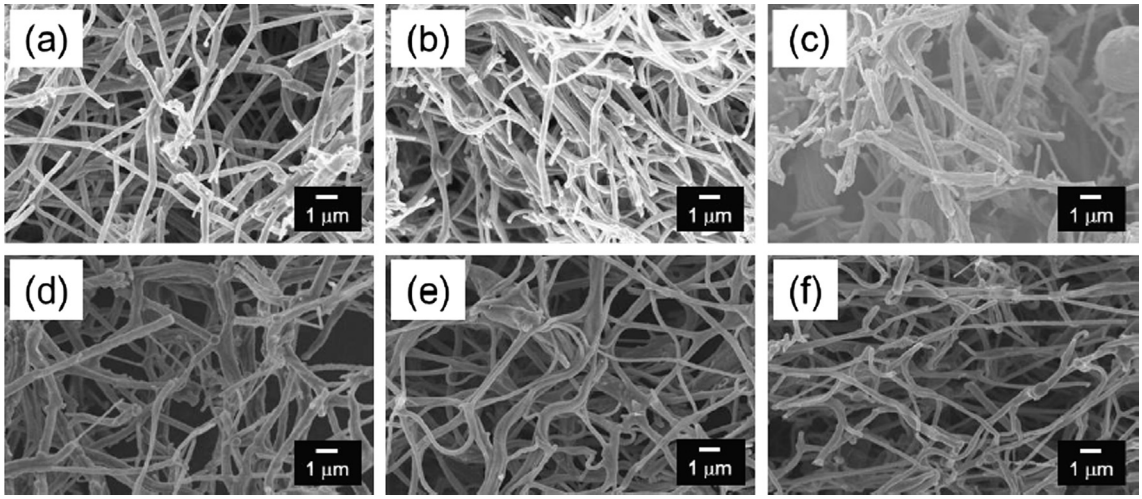

Fig. 3. SEM images of (a) $x = 0$, (b) 0.2, (c) 0.4, (d) 0.6, (e) 0.8 and (f) 1.

grounded with 5 wt% polytetrafluoroethylene powder. The mixture was spread and pressed on SUS-304 mesh. $LiClO_4$ of 1 mol dm^{-3} in EC/DEC was used as an electrolyte. Cell assembly was carried out in a glovebox under an argon atmosphere. The weight in specific capacity and current rate were calculated only for active materials. The rate performance was tested five times at five charge/discharge rates (0.05, 0.1, 0.2, 0.5 and 1.0C), respectively.

3. Results and discussion

XRD profiles and Rietveld refinement for $LiMn_xFe_{1-x}PO_4$/VGCF are shown in Fig. 1. The XRD peaks for $LiMn_xFe_{1-x}PO_4$ shift to a lower angle as x (Mn ratio) increases. For each compound, an XRD peak from VGCF was observed at around 26° [20]. The Rietveld refinement confirmed that all samples were identified as a single-phase orthorhombic olivine belonging to the space group *Pnma*. The XRD measurement revealed no impurities such as oxidation products. Moreover, the sharp XRD profiles suggest that the prepared samples have high crystallinity.

Fig. 2 shows the variation of unit cell parameters as a function of Mn content x in $LiMn_xFe_{1-x}PO_4$ obtained by the Rietveld refinement. All the parameters increase linearly with increasing x according to Vegard's law. This result indicates the successful fabrication of $LiMn_xFe_{1-x}PO_4$ for the entire compositional range $0 < x < 1$.

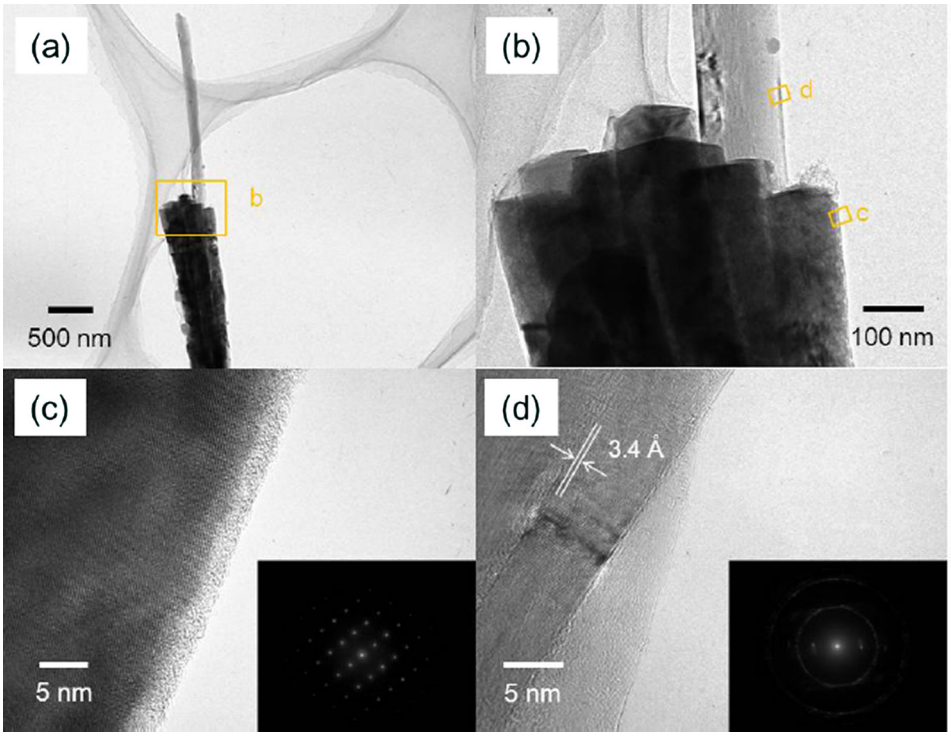

Fig. 4. TEM images for $x = 0.6$. (a) Low-magnification image. (b) Magnified part in (a). (c) Magnified part of the olivine nanowire in (b). (d) Magnified part of the VGCF in (b). The inset images show electron diffraction patterns of the olivine and VGCF, respectively.

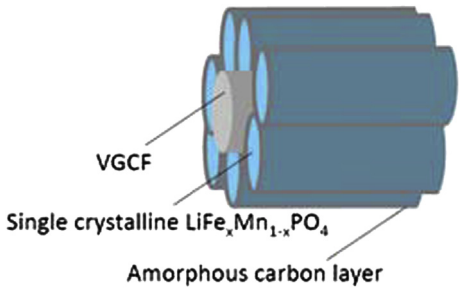

Fig. 5. Model image of $LiMn_xFe_{1-x}PO_4$/VGCF composite nanowire.

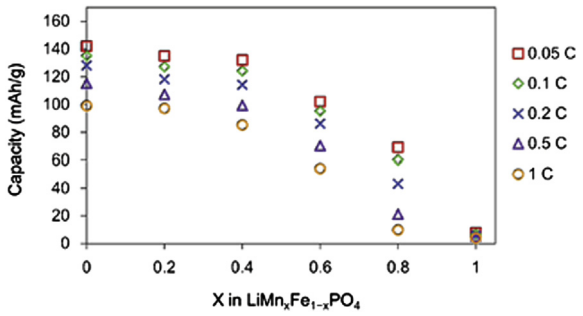

Fig. 7. Reversible specific capacities as a function of Mn content x in $LiMn_xFe_{1-x}PO_4$.

Fig. 3a–f shows FE-SEM images of the $LiMn_xFe_{1-x}PO_4$/VGCF nanowires. The nonwoven cloth structure consisting of the nanowires was observed regardless of x. The diameter of the nanowires was about 100–500 nm. Presumably, the nonwoven cloth structure leads to suppression of grain growth under high-temperature heating. VGCF cannot be distinguished clearly in the SEM images, because VGCF is incorporated into the spun nanowire as the core and uniformly dispersed.

The morphology of the $LiMn_xFe_{1-x}PO_4$/VGCF nanowires was investigated by bright-field TEM. Fig. 4 shows TEM images of $LiMn_xFe_{1-x}PO_4$/VGCF ($x = 0.6$) nanowires. Fig. 4(a, b) and (c, d) are low- and high-magnification images, respectively. Fig. 4c shows a high-magnification image of the outer sheath nanowire in (b). As shown in Fig. 4c, a lattice fringe is observed, suggesting that the part is $LiMn_{0.6}Fe_{0.4}PO_4$. The surface of $LiMn_{0.6}Fe_{0.4}PO_4$ thus seems to be coated with amorphous carbon. Fig. 4d shows the magnified part of the core nanowire in (b). The lattice fringe derived from the VGCF is observed, in which the lattice spacing is estimated to be 3.4 Å. This value corresponds to the lattice spacing estimated from the peak position for the VGCF ($2\theta = 26°$) in XRD measurement. Thin nanowires ($d \approx 100$ nm) are bundled around the VGCF to form a composite nanowire with a diameter of about 500 nm. Fig. 4b shows the magnified part in (a). The core–sheath structure, in which the core nanowire is bundled by nanowires, can be observed in this image. The inset image of Fig. 4c, which is a spot pattern of the selected area electron diffraction (SAED) pattern of $LiMn_xFe_{1-x}PO_4$ ($x = 0.6$) nanowire, indicates that a single crystal was prepared by electrospinning. The inset image of Fig. 4d represents the SAED of the VGCF, which shows clear spots perpendicular to the nanowire direction due to the interlamellar distance of the VGCF. Thus, a composite single-crystalline nanowire of $LiMn_xFe_{1-x}PO_4$ coated with a layer of amorphous carbon can be easily synthesized by the electrospinning method. The mechanism of formation of the single-crystalline nanowire is not yet completely understood, but electrospinning without VGCF has also been reported to yield single-crystalline nanowire of $LiFePO_4$ [21] and $LiMn_{0.4}Fe_{0.6}PO_4$ [20]. As shown in Fig. S1(a), some nanowires are found to consist of $LiMn_{0.6}Fe_{0.4}PO_4$ without the VGCF core. The SAED patterns for the nanowire without the VGCF core, Fig. S1(b) and (c), show clear Bragg diffractions, which indicate single crystalline nature of the nanowire.

As shown in Figs. S2–6, the core–sheath structured nanowires consisting of $LiMn_xFe_{1-x}PO_4$ nanowires and VGCF have also been confirmed in other $LiMn_xFe_{1-x}PO_4$/VGCF nanowires ($x = 0$, 0.2, 0.4, 0.8 and 1.0). Moreover, electron diffraction measurements confirmed the spot patterns derived from the single crystal, regardless of Mn content. The percentage of VGCF is around 11 wt%. Fig. S7 shows the thermogravimetric (TG) analysis of $LiMn_{0.6}Fe_{0.4}PO_4$/VGCF. The TG analysis reveals the amount of VGCF under the assumption from the second weight loss, which is ascribed to pyrolysis of VGCF in TG.

Fig. 5 shows a model image of the $LiMn_xFe_{1-x}PO_4$/VGCF core–sheath composite nanowire based on the results of TEM images. $LiMn_xFe_{1-x}PO_4$ nanowires having a diameter of about 100 nm and

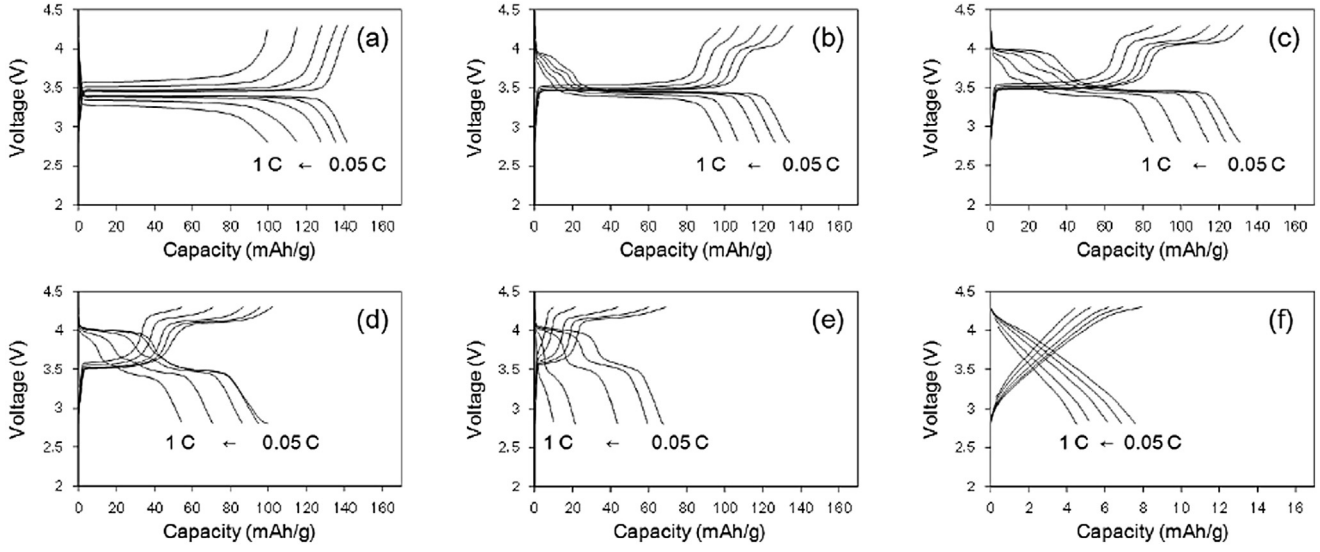

Fig. 6. Charge/discharge curves for (a) $x = 0$, (b) 0.2, (c) 0.4, (d) 0.6, (e) 0.8 and (f) 1. (Fig. 6(c) Reproduced by permission of The Royal Society of Chemistry).

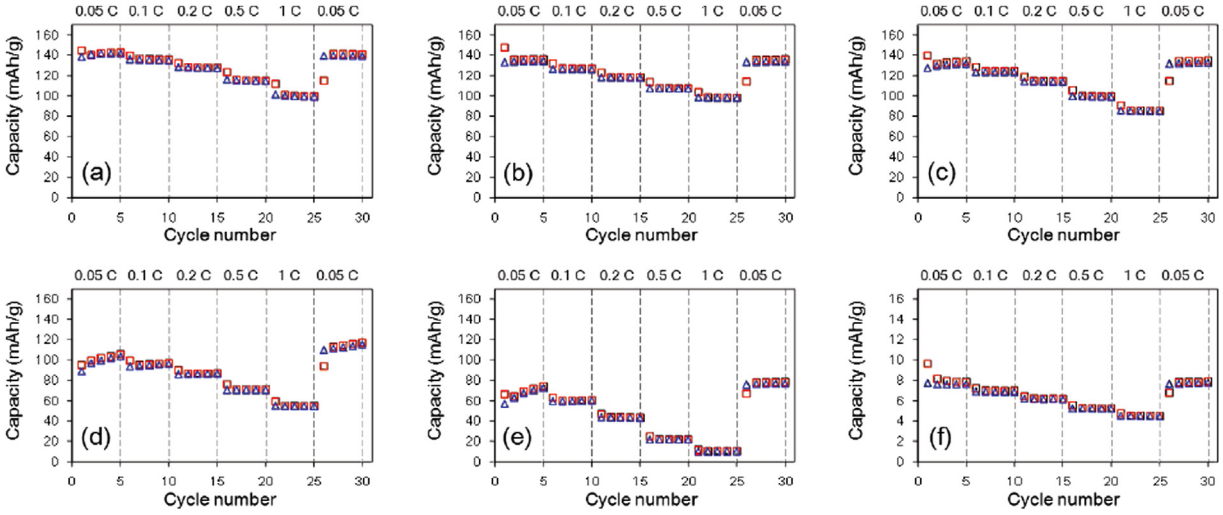

Fig. 8. Reversible capacities during continuous cycling at various charge–discharge rates for (a) $x = 0$, (b) 0.2, (c) 0.4, (d) 0.6, (e) 0.8 and (f) 1. Red squares represent charge. Blue triangles represent discharge. (For interpretation of the references to colour in this figure legend, the reader is referred to the web version of this article.)

high crystallinity are bundled around the VGCF core to form the core–sheath composite nanowires.

Fig. 6 shows the charge–discharge curves for $LiMn_xFe_{1-x}PO_4$/VGCF. In the case of $x = 0$ (Fig. 6a), a well-defined plateau assigned to Fe^{2+}/Fe^{3+} redox was observed at about 3.5 V vs. Li/Li^+ up to 1C rate. Two plateaus were observed at about 3.5 V (Fe^{2+}/Fe^{3+} redox) and about 4.1 V (Mn^{2+}/Mn^{3+} redox) vs. Li/Li^+ at 0.05C rate and gradually became sloped as the current density was increased for $x = 0.2$ (Fig. 6b), 0.4 (Fig. 6c), 0.6 (Fig. 6d) and 0.8 (Fig. 6e). Compared with the potential plateaus for $LiMn_{0.4}Fe_{0.6}PO_4$ nanowire without VGCF in our previous study, those for $LiMn_{0.4}Fe_{0.6}PO_4$/VGCF nanowire remained well defined even at 1C [20]. The reduced polarization for $LiMn_{0.4}Fe_{0.6}PO_4$/VGCF is ascribed to better electronic conductivity based on the VGCF core. On the other hand, for $x = 1$ (Fig. 6f), sloped curves were confirmed between 0.05 and 1C rate. The potential plateau does not indicate poor electronic and ionic conductivities for $LiMnPO_4$. In other words, the $LiFePO_4$ parts in $LiMn_xFe_{1-x}PO_4$ solid solution mainly act as electronic and ionic conduction paths in the material.

The specific discharge capacity as a function of Mn content x is shown in Fig. 7. The change of specific capacity with respect to x was not linear for $LiMn_xFe_{1-x}PO_4$/VGCF nanowires. The specific capacity decreased slightly up to $x = 0.4$, and then abruptly decreased at $x = 0.6$ and 0.8. In the case of $x = 1$, the capacity is only 8 mAh g^{-1}. It is considered that the change of specific capacity differs between the range of $x = 0$–0.4 and the range of $x = 0.6$–1.0 since the influence of $LiMnPO_4$ with poor electronic and ionic conductivities becomes dominant. Fig. 8 shows the discharge capacities during continuous cycling at various current densities for $LiMn_xFe_{1-x}PO_4$/VGCF. In the case of $x = 1$ (pure $LiMnPO_4$), the change of capacity is not large because the capacity at low current density is too small. $LiMn_{0.8}Fe_{0.2}PO_4$ ($x = 0.8$) and $LiMn_{0.6}Fe_{0.4}PO_4$ ($x = 0.6$) indicate large difference in the rate properties. Each capacity-retention of $LiMn_{0.8}Fe_{0.2}PO_4$ and $LiMn_{0.6}Fe_{0.4}PO_4$ from 0.05C to 1C is around 15% and 55%, respectively. When the ratio of Mn is 0.6, the capacity and rate properties are largely improved. In the case of $x = 0.4$ ($LiMn_{0.4}Fe_{0.6}PO_4$), the capacity retention is improved up to about 65%. When Mn ratio is decreased to 0.2, the capacity is approximate to that of pure $LiFePO_4$ ($x = 0$). Moreover, good rate properties (over 70%) are shown in both materials of $LiMn_{0.2}Fe_{0.8}PO_4$ and $LiFePO_4$. It is considered that the Fe ratio is important to get large capacity and good rate performance. In this experiment, VGCF acts as a good electroconductive path.

4. Conclusion

We succeeded in producing nonwoven structured $LiMn_xFe_{1-x}PO_4$ nanowire with a VGCF core column and sheaths with amorphous carbon and $LiMn_xFe_{1-x}PO_4$. It was confirmed that the $LiMn_xFe_{1-x}PO_4$ nanowire consisted of a single crystal regardless of the ratio of Mn to Fe. The charge/discharge capacities reduced with increasing Mn content owing to the poor electronic conduction path for $LiMnPO_4$. It is considered that the Fe ratio in $LiMn_xFe_{1-x}PO_4$ is important for a good performance.

Acknowledgment

This work was partially performed using facilities of the Institute for Solid State Physics, the University of Tokyo, partially conducted on the basis of the MOU between AIST, Japan, and LBNL, DOE, USA.

Appendix A. Supplementary data

Supplementary data related to this article can be found at http://dx.doi.org/10.1016/j.jpowsour.2013.09.133.

References

[1] M. Armand, J.M. Tarascon, Nature 451 (2008) 652.
[2] H. Nishide, K. Oyaizu, Science 319 (2008) 737.
[3] Y.G. Guo, J.S. Hu, L.J. Wan, Adv. Mater. 20 (2008) 2878.
[4] Y. Wang, G. Cao, Adv. Mater. 20 (2008) 2251.
[5] E. Hosono, Y.G. Wang, N. Kida, M. Enomoto, N. Kojima, M. Okubo, H. Matsuda, Y. Saito, T. Kudo, I. Honma, H.S. Zhou, ACS Appl. Mater. Interfaces 2 (2010) 212.
[6] J. Kameoka, D. Czaplewski, H. Liu, H.G. Craighead, J. Mater. Chem. 14 (2004) 1503.
[7] S.A. Sell, G.L. Bowlin, J. Mater. Chem. 18 (2008) 260.
[8] S.W. Choi, S.M. Jo, W.S. Lee, Y.R. Kim, Adv. Mater. 15 (2003) 2027.
[9] S.W. Choi, J.R. Kim, Y.R. Ahn, S.M. Jo, E.J. Cairns, Chem. Mater. 19 (2007) 104.
[10] D. Li, G. Ouyang, J.T. McCann, Y. Xia, Nano. Lett. 5 (2005) 913.
[11] A.K. Padhi, K.S. Nanjundaswamy, J.B. Goodenough, J. Electrochem. Soc. 144 (1997) 1188.
[12] K. Amine, H. Yasuda, M. Yamachi, Electrochem. Solid-State Lett. 3 (2000) 178.
[13] S. Nishimura, G. Kobayashi, K. Ohyama, R. Kanno, M. Yashima, A. Yamada, Nat. Mater. 7 (2008) 707.
[14] C. Delmas, M. Maccario, L. Croguennec, F. Le Cras, F. Weill, Nat. Mater. 7 (2008) 665.
[15] P. Gibot, M. Casas-Cabanas, L. Laffont, S. Levasseur, P. Carlach, S. Hamelet, J.-M. Tarascon, C. Masquelier, Nat. Mater. 7 (2008) 741.
[16] C. Delacourt, L. Laffont, R. Bouchet, C. Wurm, J.-B. Leriche, M. Morcrette, J.-M. Tarascon, C. Masquelier, J. Electrochem. Soc. 152 (2005) A913.

[17] A. Yamada, Y. Kudo, K.Y. Liu, J. Electrochem. Soc. 148 (2001) A747.
[18] S.-M. Oh, S.-W. Oh, C.-S. Yoon, B. Scrosati, K. Amine, Y.-K. Sun, Adv. Funct. Mater. 20 (2010) 3260.
[19] A. Yamada, Y. Kudo, K.Y. Liu, J. Electrochem. Soc. 148 (2001) A1153.
[20] K. Kagesawa, E. Hosono, M. Okubo, J. Kikkawa, D. Nishio-Hamane, T. Kudo, H.S. Zhou, CrystEngComm 15 (2013) 6638.
[21] C. Zhu, Y. Yu, L. Gu, K. Weichert, J. Maier, Angew. Chem. Int. Ed. 50 (2011) 6278.